Three-dimensional fluence rate measurement and data acquisition system for minimally invasive light therapies

Benjamin Lai,[1,2] Maxim Loshchenov,[1,3] Alexander Douplik,[1] Rob Rusnov,[1] Marcos Jimenez-Davila,[1] George Netchev,[1] and Lothar Lilge[1,2,a)]
[1]*Division of Biophysics and Bioimaging, Ontario Cancer Institute, Toronto, Canada*
[2]*Department of Medical Biophysics, University of Toronto, Toronto M5G2M9, Canada*
[3]*Institute of General Physics, Vavilova str., 38, Unit 2, 119991 Moscow, Russia*

(Received 17 September 2008; accepted 6 April 2009; published online 30 April 2009)

Light based therapies such as photodynamic therapy are in need of advanced tools for light fluence rate dosimetry and monitoring within the context of therapy planning and light delivery to ensure maximum treatment efficacy. The use of a single, multisensor fiber-based fluorescent probe capable of performing spatially resolved fluence rate measurements along an axis was demonstrated. This work extends the previous technique and describes a fluence rate quantification system able to employ up to 12 multisensor probes to simultaneously measure fluence rate distribution throughout a 3D treatment volume. The system optoelectronics provides for sensor calibration, data acquisition, and weighted least-squares processing to extract localized fluence rate information in real-time. Core components include an integrating cylinder for source sensor calibration, a 2D back thin CCD detector for sensor signal detection from multiple probes, high-speed data acquisition card, and custom software for real-time extraction of fluence rate information from all sensors. © *2009 American Institute of Physics.* [DOI: 10.1063/1.3125062]

I. INTRODUCTION

Light based therapies, such as photodynamic therapy (PDT), interstitial laser photocoagulation (ILP), and interstitial laser hyperthermia (ILH), are being investigated for various oncological and nononcological applications.[1,2] PDT employs a photosensitive drug, which, after activation with photons of a specific wavelength, generates reactive singlet oxygen destroying the target tissue, whereas ILP thermally denatures biological tissue.

Efficacy of PDT for superficial tumors is high,[3–6] but for conditions such as deep-seated tumors of the lung, brain, and prostate, requiring an interstitial PDT (IPDT) approach, efficacy appears to be reduced even when using otherwise effective and clinically approved photosensitizers such as Photofrin.[7,8]

One of the efficacy-determining factors in IPDT and other light based therapies is the distribution of the treatment light fluence rate $[H(\mathbf{r})]$ within the clinical treatment volume (CTV).[9] The current standard tool for $[H(\mathbf{r})]$ quantification is the scattering tip or cut-end fiber,[10,11] allowing quantification only at one point. Multisensor fiber-based fluorescent probes (MSPs) have emerged as an alternative tool allowing spatially resolved $[H(\mathbf{r})]$ measurements along an optical fibers' axis.[12]

This work extends the technique of using MSPs and describes a system capable of utilizing multiple MSPs (up to 12) within the CTV as shown in Fig. 1 for real-time $[H(\mathbf{r})]$ measurement throughout a three dimensional (3D) volume during IPDT and other light based therapies such as ILP (Ref. 13) and ILH.[14]

II. MATERIALS AND METHODS

A. Multisensor fiber optic probe fabrication

The MSP design shown in Fig. 2 has been described by Pomerleau-Dalcourt and Lilge.[12] Physical dimensions are the

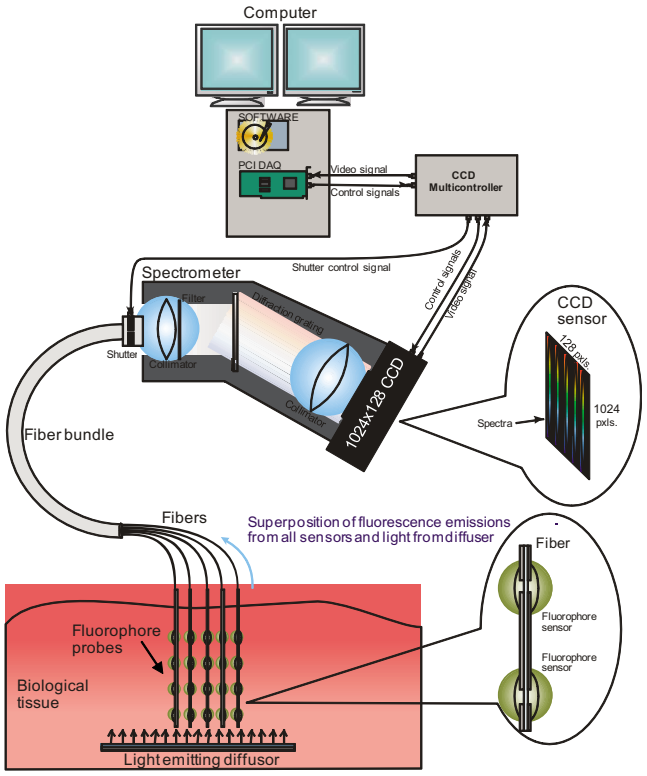

FIG. 1. (Color online) Block diagram of the optoelectronic setup used for multisensor fluence rate probe quantification.

a)Electronic mail: llilge@uhnres.utoronto.ca.

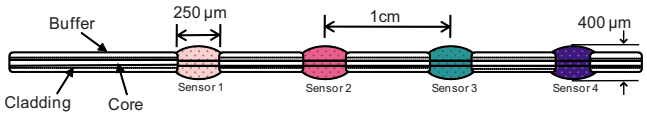

FIG. 2. (Color online) Schematic diagram of the fabricated fiber probe with sensors placed on the etched grooves.

same; however FG silica multimode fibers (FG200LCC, Thorlabs, NJ, USA), requiring a different manufacturing approach, were chosen in this work for their higher transmission in the visible to NIR range and reduced optical crosstalk between sensors on the probe.

250 μm long sections of the outer plastic buffer layer were removed at preselected positions with a microlathe. The exposed silica cladding layer was dissolved over 24 min by hydrofluoric acid (HF) wet etching, resulting in grooves having a very smooth surface exposing the fiber core. A selection of fluorophores diluted to 2.5 mM concentration in methanol was individually mixed with a UV-curing medical epoxy (141-M, DYMAX, Torrington, CT) in a 4:1 epoxy: fluorophore ratio (v/v) to prevent fluorophore aggregation upon curing. The prepared mixtures were placed into the grooves to form sensors and cured under UV light source (5 cm distance) for 30 s and annealed over 24 h at 60 °C.

B. Fluorophore selection and characterization

Here a treatment wavelength of 670 nm was selected as required for tin etiopurpurin dichloride $SnET_2$ (Frontier Scientific, Inc., Logan, UT) mediated PDT.[15] Thirteen candidate fluorophores with absorption at 670 nm were considered (see Table I) and evaluated on their emission profiles and stability under high fluence rate exposure.

The spectral similarities between these $K=13$ fluorophores were assessed by examining the wavelength dependent orthogonality of all fluorescence emission pairs, resulting in a $K \times K$ matrix. Summation of the matrix rows assigned a uniqueness score to each candidate fluorophore as a comparison metric.

TABLE I. Candidate fluorophores uniqueness scores, responsivity decay factors, and their assigned code letters used to identify them in this paper. Vendor names are abbreviated as follows: 1, Exciton Inc., Dayton, OH, USA and 2, American Dye Source, Inc., Baie D'Urfe, Que, CA.

Code	Dye name	Vendor	Uniqueness score	Decay factor (cm^2/J)
A	LDS867	2	1.266 96	1.00E-04
B	ADS640PP	1	1.376 03	3.00E-05
C	ADS680BP	1	1.264 23	···
D	ADS680HO	1	1.955 18	3.00E-04
F	LDS 821	2	3.266 58	···
G	LD 700	2	1.461 17	···
J	ADS760MP	1	1.266 96	1.70E-03
L	LDS 800	2	1.899 34	···
N	Nile Blue 690 Perchlorate	2	1.933 99	1.00E-04
P	ADS745HT	1	6.176 73	1.10E-03
X	Oxazine 725	2	1.685 37	···
Y	Oxazine 750	2	1.831 14	···
Z	ADS680WS	1	1.1583	···

Photostability of the candidate fluorophores was verified under direct illumination by 670 nm light at 38 mW cm^{-2} (3 mm diameter spot size) irradiance over 20 min, delivering 45.6 J cm^{-2} radiant exposure. This exceeds the threshold required for tissue necrosis by close to a factor of ten for most photosensitizers and target tissue combinations. A reflectance probe (silica fiber, 200 μm, Biospec, Moscow, Russia) connected to a 670 nm diode laser and a spectrometer (MSL-CS1-USB-VIS, MedSpecLab, Toronto, ON, Canada) delivered excitation and tracked emissions, respectively. Bleaching rates were determined from the ratio of the wavelength-integrated fluorescence emission spectrum above 690 nm to that taken at the onset of irradiation and plotted as a function of radiant exposure.

C. Integrating cylinder for probe calibration

An integrating cylinder [Fig. 3(a)] with a 34 mm diameter cavity, 65 mm length, and at least 1 cm wall thickness was constructed from ultrahigh density polyurethane (Gigahertz, Munich, Germany). Three equidistant light delivery ports tilted 14° against the cylinder's short axis provide uniform illumination. A multiplication factor of 38 was measured experimentally. Unique to the design is an opaque ceramic tube coated with barium sulfoxide $BaSO_4$ (Kodak, Rochester, NY, USA) with a 5 mm slit in the center and a clear glass capillary (Wilmad, Buena, NJ, USA) both mounted along the long axis for probe calibration.

During calibration the cylinder provides a known fluence rate. The probe inserted into the ceramic tube is withdrawn by a stepper motor, and all sensors move sequentially across the slit, exposing them to the excitation light as shown in Fig. 3(b). This provides $F_i(\lambda)$, the sensor-specific emission profile. Thus, generated calibration map containing emission profiles for all sensors of a given probe as a function of fiber position and wavelengths is plotted in Fig. 3(c). As the slit does not allow for exposure over a full solid angle ($4\pi sr$), the probe is irradiated again in the glass capillary for absolute responsivity calibration of all sensors using known fluence rates within the integrating cylinder.

D. Spectrometer for multifiber detection

Up to 12 MSPs are connected to a fiber bundle, aligned 400 μm center-to-center, and connected proximally to a spectrophotometer. The spectrophotometer (P&P Optica, Kitchener Waterloo, ON, Canada) features a transmission volume phase holographic grating for wavelength separation and permits the emission of up to 12 spectra from the fiber probes to be simultaneously imaged along the short axis of a two-dimensional charged coupled device (2D-CCD) detector (S7031–1007, Hamamatsu, NJ, USA). A high-speed data acquisition (DAQ) card (6036E, National Instruments, TX, USA) acquires the optical signals from all probes for software processing. Custom software performs a weighted least-squares (LS) decomposition (see Appendix) for each probe to recover the localized fluence rates at each sensor position. The recovered data are used to reconstruct the fluence rate distribution in the measured volume.

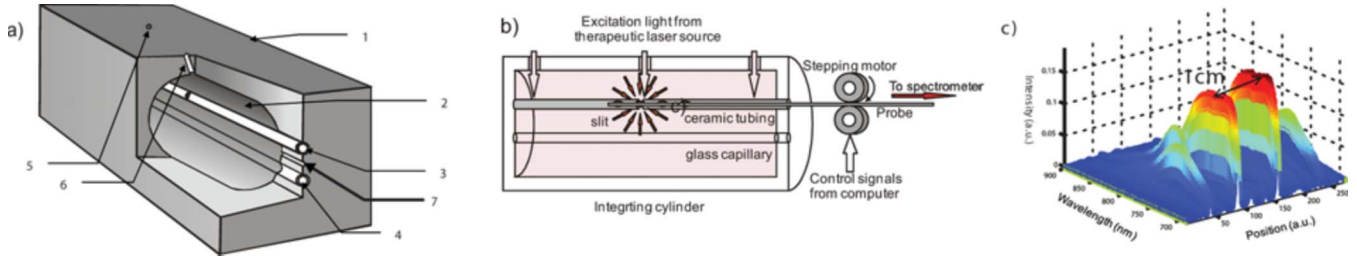

FIG. 3. (Color online) (a) 3D view of the integrating cylinder. 1: polyurethane case; 2: cylindrical cavity; 3: ceramic tubing with slit for individual sensor exposure; 4: glass tubing for absolute fluence rate calibration; 5 and 6: light delivery ports; 7: monitoring port. (b) Diagram illustrating automatic calibration mode using a computer controlled stepper motor. (c) Resulting 3D intensity map of measured spectra.

III. RESULTS AND DISCUSSION

A. Fluorophore uniqueness scores and photostability

Table I shows the uniqueness scores for all candidate fluorophores, where a low score indicates greater distinctiveness. Scores between 1.0 and 2.0 indicate potential sensor fluorophores.

Fluorophores that bleached significantly due to UV exposure for adhesive polymerization were discarded, while the remaining candidates underwent photostability testing. All fluorophores exhibited reduced emission intensities as a function of radiant exposure (J cm^{-2}) demonstrated in Fig. 4(a) for fluorophore J at 0 J cm^{-2} and after 45.6 J cm^{-2}. The intensity decrease follows the exponential e^{-kf} relationship, where f is the deposited energy radiance and k is the responsivity decay factor, see Fig. 4(b). Table I lists k for applicable fluorophores recovered with an exponential fit having R^2 values above 0.95. Because the excitation source is constant during exposure, the responsivity decay factor describes how a sensor increasingly underestimates the true fluence rate with higher fluence.

Three fluorophores, J, P, and B, were chosen as sensors based on the established criteria. Figure 5 shows the normalized emission spectra for the three sensors. While fluorophore P had one of the highest uniqueness scores, its lowest responsivity decay factor and high orthogonality relative to fluorophores J and B resulted in its inclusion.

B. Fluence rate homogeneity inside the integrating cylinder

Figure 6 shows the relative fluence rate across the long axis of the cylinder. The region of interest for sensor responsivity calibration extends from positions 15–80 mm from the distal end of the cylinder as it corresponds to the inner cavity. The temporal variation in fluence rate across this region at each position for repeat measurements is less than 1%. The overall spatial variation in illumination over this distance is 1.6%

C. Validation of the software LS decomposition algorithm and determination of cross-talk

Probes with sensors B, J, and P at the distal, proximal, and middle positions, respectively, were constructed and calibrated. Sensors on the probe were illuminated randomly one at a time, and the LS decomposition algorithm deter-

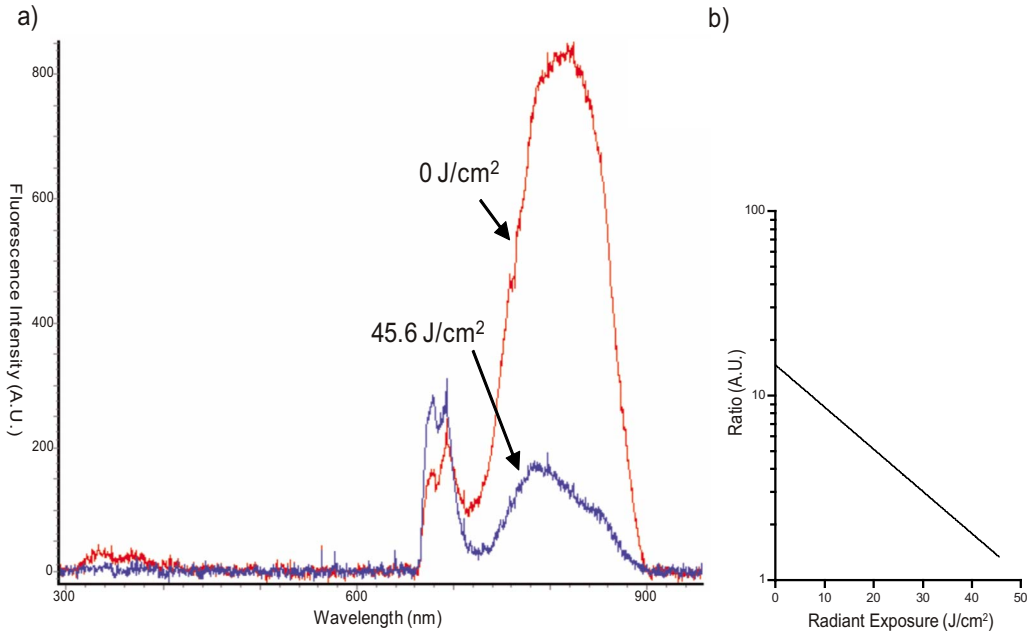

FIG. 4. (Color online) (a) Fluorophore emission intensity at the 0 J/cm^2 and 45.6 J/cm^2 of photostability test. (b) Exponential behavior of the ratio between area under initial fluorescence spectrum and the measured spectrum as a function of increasing radiant exposure.

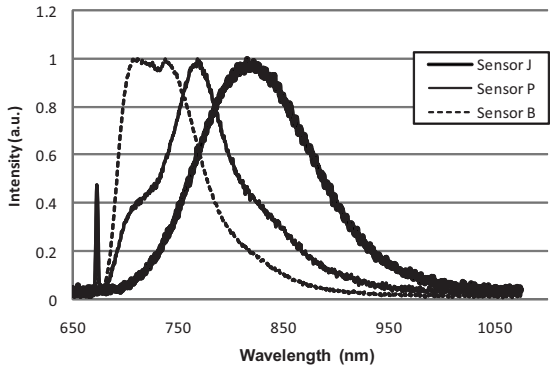

FIG. 5. Normalized fluorescence spectra of the chosen fluorophores.

mined the contributions of each sensor and identified the irradiated sensor as shown in Table II. The cleaved distal tip of the probe was also illuminated to demonstrate that the excitation light (670 nm) coupled into the fiber core does not induce excitations of the fluorophore sensors as shown by the last row of Table II, thus indicating the absence of cross-talk between sensors.

The possibility of cross-talk between MSPs was also considered and was found to be negligible. For probes positioned 1 cm apart similar to the configuration described by Li and Zhu[16] for the prostate, light attenuation in the tissue exceeding and optical density of 2 prevents sensor fluorescence affecting neighboring probes. During exposure of the CCD, the spectral images from each MSP are sufficiently separated to prevent cross-talk. This was confirmed by examining the CCD counts of the pixel regions between MSP images. Levels are comparable to those acquired during dark measurement.

D. Overall system accuracy

Medical devices regulations (AAPM Task Group 140, publication pending) require that optical power meters be National Institute for Standards and Testing (NISI) traceable and calibrated to within 10% of the true optical power for treatments such as PDT. Results from the validation experiments were analyzed to quantify the uncertainty, as various

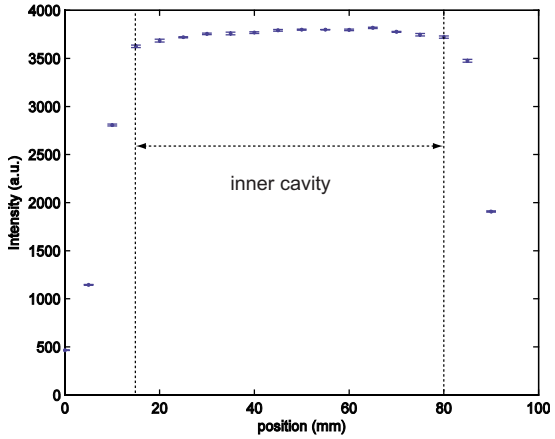

FIG. 6. (Color online) Light intensity along the major axis of the integrating cylinder.

TABLE II. Recovered sensor contributions from the LS validation test.

	Recovered coefficients			
Illuminating	C_B	C_P	C_J	C_{laser}
Sensor B	0.054	0	0	0
Sensor P	0	0.044	0	0
Sensor J	0	0.004	0.281	−0.002
Fiber tip	0	0	0	0.091

system components (sensors, integrating cylinder, and the LS algorithm) contribute to the quantified fluence rate and its errors.

The first error source stems from the sensors' response to prolonged irradiation, resulting in an underestimation of the actual fluence rate. Assuming that the threshold fluence to induce necrosis of surrounding healthy tissue is 10 J cm^{-2} or less,[15,17–19] the true fluence will be underestimated based on the responsivity decay model by 0.03%, 1.09%, and 0.10% for sensors B, P, and J, respectively.

Variations in the fluence rate along the length of the cylinder would contribute an additional error in fluence quantification. The measured variation in relative fluence along the region of interest inside the cylinder does not exceed 1.6%.

The LS decomposition can provide an additional source of errors but can be analyzed using results similar to Table II. The LS error contribution is inclusive of all electronic noise and DAQ sampling errors as all data presented to the LS algorithm for processing contain them implicitly. For each individual experiment the percent error is determined according to

$$\text{error} = \left(1 - \frac{C_{\text{sensor}}}{\sum_{i=1}^{K+1} |C_i|}\right) \times 100, \tag{1}$$

where C_{sensor} is the contribution of the sensor being illuminated, while $\Sigma_{i=1}^{K+1} C_i$ is the sum of all recovered coefficients reported by LS. For example, when $\Sigma_{i=1}^{K+1} |C_i| = C_{\text{sensor}}$, 100% of the contributions come from a single source: the sensor being illuminated. From this analysis, it follows that the overall LS processing error is 2.09%. As additional sensors can be selected and added to the probe to gain spatial fluence rate resolution, the LS decomposition error is expected to increase as the overall system complexity goes up. The errors introduced with additional sensors depend on the spectral relationship between sensors (orthogonality), as well as the location of their emission peaks (an issue of signal to noise) since the CCD is not equally sensitive at all wavelengths.

The total system uncertainty is the sum of the uncertainties of each system component. Even when considering the largest uncertainty of each component, the overall system uncertainty is approximately 4.8%, still well below the 10% limit proposed for optical power meters in PDT according to AAPM Task Group 140.

IV. CONCLUSION

A system for real-time spatially resolved fluence rate quantification and optical probe calibration was described and demonstrated. A three-sensor fiber probe was fabricated to show that the system operates well within the AAPM guidelines. Spatial resolution may be improved by increasing the number of sensors used, though they must have low uniqueness scores to be resolved by the LS algorithm. The responsivity of the optical sensors could be enhanced by substituting fluorescent nanoparticles for fluorophores since they are inherently resistant to photodegradation.[20] This may be particularly useful in high irradiance environments found in ILP and ILH.

ACKNOWLEDGMENTS

The authors acknowledge financial support in part by CIHR Grant No. 68951 and NIH Grant No. PO1CA 43892. One of the authors (B.L.) would like to acknowledge partial funding through the OSOTF Scace, Starita, and Cunningham Fellowships from the University of Toronto.

APPENDIX: SPECTRAL DECOMPOSITION ALGORITHM USING A WEIGHTED LS TECHNIQUE

For each probe the detected spectrum $S(\lambda)$ is the sum of individual fluorophore contributions, $F_i(\lambda)$, for a known standard calibration fluence rate, multiplied by a coefficient C_i, indicating their relative contribution. The laser line is also considered an independent contribution to minimize its interference during decomposition. LS minimization is performed for each probe to recover the sensor contributions C_i.

Under standard LS, minimization is performed $K+1$ times for K sensors plus the laser line. Each minimization is computed with respect to the jth coefficient C_j, with $j \in [1 \ldots K+1]$. A weighting function is introduced to suppress wavelengths where overlap exists between the spectral components of at least two fluorophore spectra. This function is based on the determinant $d(\lambda)$ of the inner product matrix $\Gamma_{ij}=\Sigma_\lambda F_i(\lambda)F_j(\lambda)$, over a sufficiently small wavelength range δ centered around λ' or $\lambda' \pm \delta/2$.

The wavelength dependence of $d(\lambda)$ becomes the weighting function $w(\lambda)=F[d(\lambda)]$ and is incorporated to the LS scheme to suppress overlapping spectral ranges to emphasize orthogonal product regions to increase the likelihood of obtaining an absolute minimum.

[1] D. E. Dolmans and R. K. Jain, Nat. Rev. Cancer **3**, 380 (2003).
[2] T. J. Dougherty, J. Clin. Laser Med. Surg. **20**, 3 (2002).
[3] C. A. Morton, S. B. Brown, S. Collins, S. Ibbotson, H. Jenkinson, H. Kurwa, K. Langmack, K. Mckenna, H. Moseley, and A. D. Pearse, Br. J. Dermatol. **146**, 552 (2002).
[4] B. F. Overholt, M. Panjehpour, and D. L. Halberg, Gastrointest. Endosc. **58**, 183 (2003).
[5] P. Grosjean, J. F. Savary, G. Wagnières, J. Mizeret, A. Woodtli, J. F. Theumann, C. Fontolliet, H. Bergh, and P. Monnier, Lasers Med. Sci. **11**, 227 (1996).
[6] S. B. Brown, E. A. Brown, and I. Walker, Lancet Oncol. **5**, 497 (2004).
[7] L. K. Lee, C. Whitehurst, Q. Chen, M. L. Pantelides, F. W. Hetzel, and J. V. Moore, Br. J. Urol. **80**, 898 (1997).
[8] V. G. Schweitzer, Lasers Surg. Med. **29**, 305 (2001).
[9] B. C. Wilson, M. S. Patterson, and L. Lilge, Lasers Med. Sci. **12**, 182 (1997).
[10] T. C. Zhu, J. C. Finlay, and S. M. Hahn, J. Photochem. Photobiol., B **79**, 231 (2005).
[11] J. P. A. Marijnissen and W. M. Star, Lasers Med. Sci. **2**, 235 (1987).
[12] N. Pomerleau-Dalcourt and L. Lilge, Phys. Med. Biol. **51**, 1929 (2006).
[13] G. Amabile, M. Rotondi, G. De Chiara, A. Silvestri, B. Di Filippo, A. Bellastella, and L. Chiovato, Thyroid **16**, 749 (2006).
[14] D. S. Robinson, J. M. Parel, D. B. Denham, X. Gonzalez-Cirre, F. Manns, P. L. Milne, R. D. Schachner, A. J. Herron, J. Comander, and G. Hauptmann, J. Am. Coll. Surg. **186**, 284 (1998).
[15] L. Lilge, N. Pomerleau-Dalcourt, A. Douplik, S. H. Selman, R. W. Keck, M. Szkudlarek, M. Pestka, and J. Jankun, Phys. Med. Biol. **49**, 3209 (2004).
[16] J. Li and T. C. Zhu, Phys. Med. Biol. **53**, 2103 (2008).
[17] L. Lilge and B. C. Wilson, J. Clin. Laser Med. Surg. **16**, 81 (1998).
[18] K. K. H. Wang, S. Mitra, and T. H. Foster, Med. Phys. **35**, 3518 (2008).
[19] J. Ferreira, L. T. Moriyama, C. Kurachi, C. Sibata, O. Castro e Silva, S. Zucoloto, and V. S. Bagnato, Laser Phys. Lett. **4**, 469 (2007).
[20] W. C. W. Chan, D. J. Maxwell, X. H. Gao, R. E. Bailey, M. Y. Han, and S. M. Nie, Curr. Opin. Biotechnol. **13**, 40 (2002).